

Ion-Mobility Spectrometry of Nickel Nanoparticle Oxidation Kinetics: Application to Energetic Materials

Lei Zhou, Ashish Rai, Nicholas Piekiet, Xiaofei Ma, and Michael R. Zachariah

J. Phys. Chem. C, **2008**, 112 (42), 16209-16218 • DOI: 10.1021/jp711235a • Publication Date (Web): 25 September 2008

Downloaded from <http://pubs.acs.org> on December 5, 2008

More About This Article

Additional resources and features associated with this article are available within the HTML version:

- Supporting Information
- Access to high resolution figures
- Links to articles and content related to this article
- Copyright permission to reproduce figures and/or text from this article

[View the Full Text HTML](#)

Ion-Mobility Spectrometry of Nickel Nanoparticle Oxidation Kinetics: Application to Energetic Materials

Lei Zhou, Ashish Rai, Nicholas Piekil, Xiaofei Ma, and Michael R. Zachariah*

Department of Mechanical Engineering and Department of Chemistry and Biochemistry University of Maryland, College Park, Maryland 20742

Received: November 27, 2007; Revised Manuscript Received: May 16, 2008

Nanoscaled nickel particles have attracted interest for their potential use as a fuel in energetic materials. In this work, we combined two ion-mobility spectrometry approaches, tandem differential mobility analysis (TDMA) and tandem differential mobility–particle mass analysis (DMA-APM), to study the size-resolved reactivity of nickel nanoparticles. Nickel nanoparticles were generated in situ by using gas-phase thermal pyrolysis of nickel carbonyl. Four particle sizes (40, 62, 81, and 96 nm, mobility size) were then selected by using a differential mobility analyzer. These particles were sequentially oxidized in a flow reactor at various temperatures (25–1100 °C). The size and mass change of the size-selected and -reacted particles were then measured by a second DMA, or an APM. We found that both particle size and mass were increased as the temperature increased. However, at higher temperature (600–1100 °C), a different mass and size change behavior was observed that could be attributed to a phase transition between NiO and Ni₂O₃. A shrinking core model employed to extract the size-resolved kinetic parameters shows that the activation energy for oxidation decreased with decreasing particle size. The burning time power dependence on particle size was found to be less than 2 and nickel particles were found to be kinetically more active than aluminum.

Introduction

Recent advancements in the field of so-called “nanoenergetic” materials are focused on either enhancing or tuning reactivity. On one level this issue reduces to a length-scale argument, whereby smaller fuel/oxidizer combinations result in smaller diffusion lengths and therefore higher reactivity. On another level, this discussion leads to choices of different thermite formulation. Although there have been considerable successes in enhancing the energy release rate of thermite systems, the goal of tuning the reactivity is still a subject for further research. In one of our previous works, we reported a method to control the energy release rate of energetic nanoparticles by creation of a core shell nanostructure on the oxidizer particle.¹ Similarly, the reactivity of nanoenergetic material can also be controlled by modifying the structure of the aluminum fuel.² More recently we have seen that mixtures of nanoaluminum and nanoboron outperform either material on their own.³ Those results suggest both material choices (e.g., Ni, Ti, etc.) and nanoarchitecture as a means to tune the energy release profiles of materials beyond aluminum. The application of those materials would take the form of composite materials, e.g., Al/Ni alloy, or metal particles with a different morphology such as aluminum core with nickel coating. While considerable opportunity exists for improvements, in actuality very little attention has been paid to the kinetics of reactivity of small metal particles beyond nanoaluminum. While the oxidation of nickel in the form of bulk sample or thin films has been studied for over a century,^{4–27} there are only a few studies on the oxidation of nickel nanoparticles.^{5,28–32} Carter developed a solid state kinetic model based on a diffusion-controlled mechanism for the oxidation of ~100 μm particles using a microbalance.²² Fromhold obtained the same oxidation rate law using a coupled current approach with the assumption of zero space charge.⁶ Karmhag and

Niklasson explored the oxidation kinetics of micron size nickel particles using thermogravimetric measurements, and obtained a lower activation energy than bulk nickel.^{31,32} As particle size decreases into the nanoscale, the mass transfer limitations should be reduced and we should expect to see an enhancement in reactivity. Our previous work on the oxidation of nanoaluminum particles shows that both the overall rate constant and activation energy are size dependent.^{33,34} Karmhag et al. studied the oxidation of nano-sized nickel particles at low temperatures (135–235 °C) using thermogravimetric measurements and suggested that nonlinear diffusion resulting from space and local charging occurs in this case, and results in a higher rate constant and lower activation energy.²⁹ The same group also probed the size-dependent oxidation kinetics, and found that the rate constant roughly goes as the square of the inverse of particle diameter.³⁰ They further proposed a phenomenological model to consider the nonlinear effect in oxidation of nanoscaled particles.²⁸

All the above studies were carried out with use of conventional dynamic thermal techniques such as thermogravimetry. It is well-known that those methods are greatly influenced by heat and mass transfer effects such that the results are biased by experimental artifacts.^{34,35} In this work we employ aerosol-based techniques to study the oxidation kinetics of Ni nanoparticles. Our previous results on the study of solid–gas phase reaction kinetics show that the reaction rates obtained using aerosol-based techniques are much higher than those from conventional methods, which may represent the intrinsic reactivity of nanoparticles.^{34,35}

The basic idea of the experimental approach is to prepare Ni particles of characterized size/shape (i.e., monodisperse) and monitor changes during oxidation in free-flight (i.e., no substrate). This study consists of two experiments, both of which rely on ion-mobility separation. A Tandem Differential Mobility Analyzer (DMA) system^{12,36,37} is used to measure the size

* Corresponding author. E-mail: m rz@umd.edu.

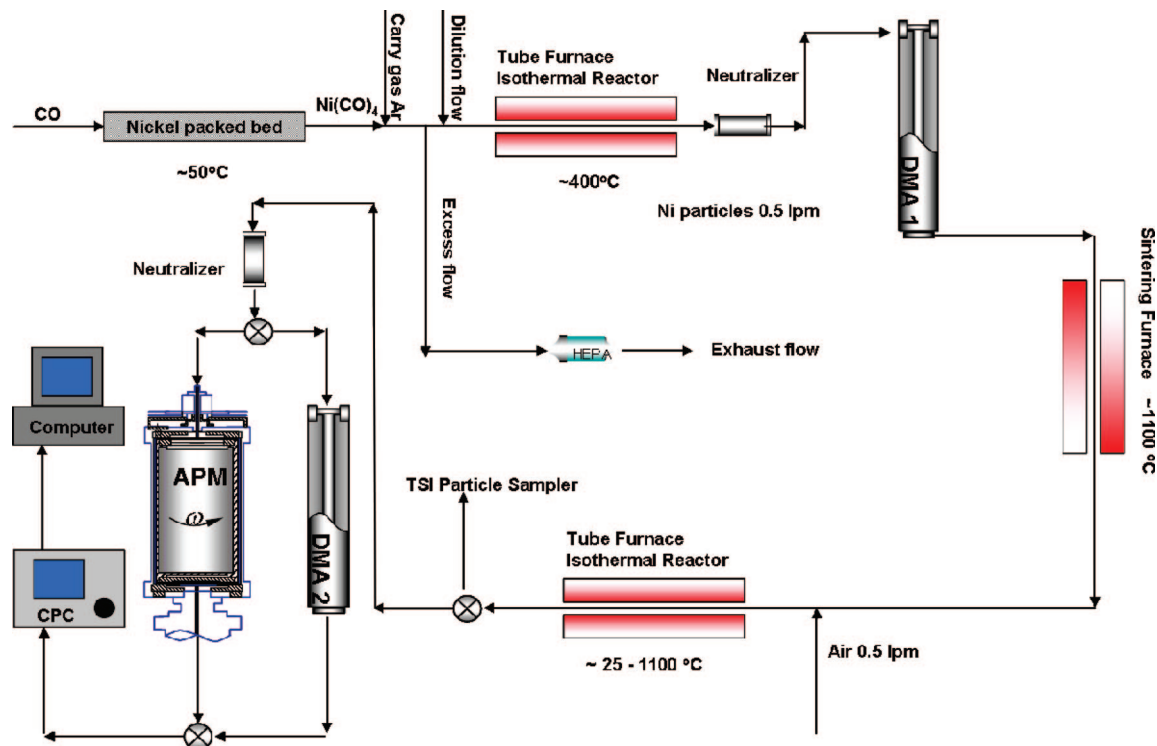


Figure 1. Schematic of Ni generation, size selection, sintering, oxidation and subsequent size, and mass measurement.

change after oxidation, while the mass change is tracked by a DMA-APM (Aerosol Particle Mass Analyzer) system.^{33,38–40} The mass and size changes of nanoparticles are studied from room temperature to 1100 °C. The average density obtained from mass and size measurements shows the nickel nanoparticle oxidation process can be correlated to the formation of both NiO and Ni₂O₃ ($4\text{Ni} + 3\text{O}_2 \rightarrow 2\text{Ni}_2\text{O}_3$, $2\text{Ni} + \text{O}_2 \rightarrow 2\text{NiO}$) and a phase change region where both the oxidation of nickel and decomposition of Ni₂O₃ to NiO ($2\text{Ni}_2\text{O}_3 \rightarrow 4\text{NiO} + \text{O}_2$) occur simultaneously. The reaction rates were then extracted from the experiment data as a function of particle size.

Experimental Approach

The experiment system consists of three components: first, preparation of monodisperse nickel particles; second, exposure of size-selected nickel particles into a controlled oxidation region; and third, measurement of the size and mass change resulting from reaction. A complete schematic of the experimental setup with temperature and flow rate control is shown in Figure 1.

A. In Situ Generation of Nickel Nanoparticles. In this work, high-purity nickel nanoparticles were prepared in an oxygen-free environment by using gas-phase thermal pyrolysis of nickel carbonyl.^{41,42} Because of the high toxicity of nickel carbonyl, it was generated in situ by flowing of a small amount of carbon monoxide (99.5%) through a nickel powder bed (3 μm, 99.7% Sigma Aldrich), which was placed immediately upstream of an isothermal tube reactor to thermally decompose Ni(CO)₄ so as to form nickel particles as shown in Figure 1. Before each experiment, the nickel bed was heated to ~350 °C with a hydrogen flow (99.5%) for about 4 h to clean the surface of the nickel powder. After the hydrogen pretreatment, activated nickel powder is reacted with CO at ~50 °C to generate Ni(CO)₄. The generated Ni(CO)₄ was mixed with a flow of Ar (industrial grade) and passed to the cracking reactor held at ~400 °C to create nickel particles ($\text{Ni(CO)}_4 \rightarrow \text{Ni} + 4\text{CO}$).

Since the resulting particles are agglomerated and our experimental protocol requires individual primary particles, the generated nickel particles were size selected by the first DMA (to be described below), and subsequently heated to 1100 °C to form spherical particles, so as to prepare monodisperse particles for the oxidation step.

B. Differential Mobility Analyzer (DMA) and Aerosol Particle Mass Analyzer (APM). The primary analytical tools employed in the experiments were a tandem differential mobility analyzer system (TDMA)^{12,36,37,43,44} and DMA-APM (aerosol particle mass analyzer) systems.^{33,38–40} In these experiments, particles were first charged with a Boltzmann charge distribution by exposing the aerosol to a Po-210 radiation source, before the first DMA. The average charge state of sample particles under Boltzmann distribution is roughly neutral, with most of particles uncharged and an equal number of particles carrying ±1 charge and ±2 charges, etc. For example, in the case of 50 nm particles, 60.2% particles will be neutral, 19.3% carry ±1 charge, 0.6% carry ±2 charges, and a higher charge state would be even less.⁴⁵ Considering the small percentage in the multiple charged states, we ignore multiple charged particles and assume the charged particles are all singly charged. Both the DMA and APM are configured to classify positively charged particles for these experiments.

The TDMA system setup was similar to that in our previous work.^{36,37,43,44} The DMA consists of an annular region between two concentric cylinders, with the center cylinder held at high voltage and the outer one at ground. Charged particles of the right polarity feel an attractive force toward the center electrode and move radially inward at an electrophoretic velocity determined by the particle charge and the particle size dependent drag force. When charged particles flow within the annular region the electric force on the particle is balanced by the drag force, and at a fixed voltage all particles exiting the instrument have equivalent mobility sizes (equivalent projected surface area). By scanning the voltage a range of particle sizes can be

extracted and counted to yield a size distribution. In our system, DMA-1 is held at a fixed voltage, and thus is used as a band-pass filter to create the monodisperse particle source, by selecting particles with the same electrical mobility size. In the size range of consideration here, the DMA functions as a source of monoarea particles.⁴⁶ However, since DMA-1 selected particles are aggregates, a sintering furnace was placed after DMA-1 to form individual spherical particles for the oxidation step. A second DMA was operated in voltage-step mode with a condensation particle counter (CPC) as a particle size distribution measurement tool to track the size change after the oxidation process. A second Po-210 neutralizer was placed between the oxidation furnace and DMA-2 to recharge the particles. This was necessary as with the high-temperature treatment (sintering or high oxidation temperatures) some of the particles lost their charge. In summary, the TDMA experiment tracks changes in physical size as a result of oxidation.

In a parallel experiment the change in particle mass after oxidation was measured by an aerosol particle mass analyzer (APM) coupled with a CPC. The APM is a relatively new technique that can determine the particle mass distribution based on particle mass to charge ratio.⁴⁰ The APM consists of two concentric cylindrical electrodes that rotate together at a controlled speed. An electrical field is created by applying high voltage on the inner electrode while the outer one is held at ground. Charged particles flowing within the concentric cylinders experience opposing centrifugal and electrostatic forces and as a result particles exiting the instrument at fixed voltage and rotation speed all have the same nominal mass. By scanning either the voltage or the rotation speed, the particle mass distribution (independent of particle shape) can be determined. Our previous experiments have used the DMA-APM technique to measure the inherent density of nanoparticles, as well as to study the mechanism of aluminum oxidation.^{33,38}

On the basis of operating conditions for the DMA and APM we estimate uncertainties as follows. For the DMA operating conditions the uncertainty is based on the theoretical transfer function, which will give an uncertainty in the peak particle size of $\pm 4\%$. We then use Gaussian fit to determine the peak size, which would have a precision uncertainty of no more than 1%. A similar result can be obtained for the APM; however, the uncertainties are not due to the transfer function but uncertainties in the step voltage, which has a resolution of only ± 0.5 V, which gives an uncertainty in mass of $\sim 4\%$.

Using the root-sum-square (RSS) method, we can estimate the uncertainty of density calculation at $\sim 5\%$. This is consistent with prior work (unpublished) using combined DMA/APM on reference aerosols (NaCl and DOP) which gave an experimentally determined uncertainty in density of 4%.

C. Nickel Nanoparticle Characterization, Sampling, and Oxidation. In this study, nickel nanoparticles with mobility sizes of 70, 135, 200, and 240 nm were selected by using the first DMA. To successfully measure the size and mass change resulting from oxidation with Tandem DMA and the DMA-APM system, the particle number concentration in the selected size range must be tuned. This is accomplished by varying the concentration of $\text{Ni}(\text{CO})_4$ in the various dilution steps used. The Ar carrier gas flow varied from 2 LPM (liter per minute) to 10 LPM, and the dilution Ar flow varied from 0.2 LPM to 0.45 LPM. Figure 2 shows an example size distribution taken before the sintering furnace. The system in this case was tuned to create a peak mobility size of about 120 nm, with sufficient particles for further measurement at the size range from 70 to 240 nm.

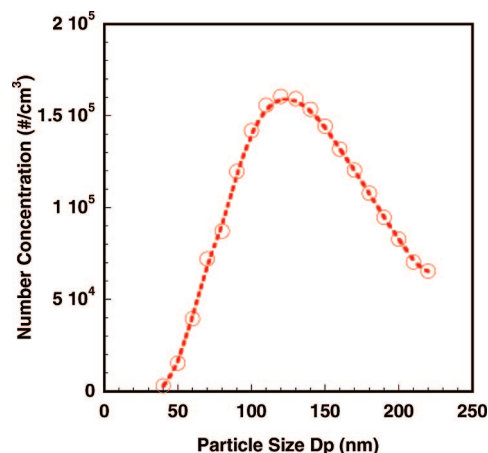


Figure 2. Single DMA scan of the overall nickel particle size distribution sampled before sintering. (The circles are the data points and the dash line is the smooth fit to the data.)

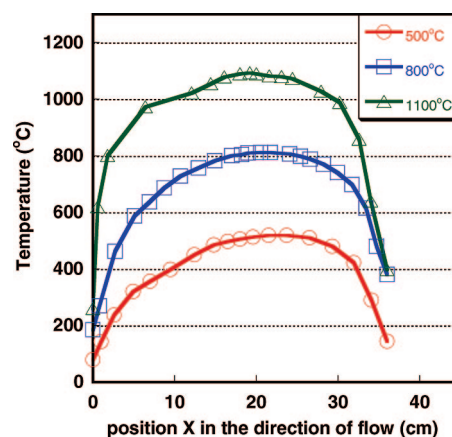


Figure 3. Temperature profile within the quartz flow tube for furnace settings of 500, 800, and 1100 °C.

Size-selected nickel particles coming from DMA-1 were subsequently sintered at 1100 °C to form monodisperse spherical particles, whose size and mass can be measured by DMA-2 and APM, under condition of no oxidation. The size of particles shrinks to a mobility size of 40, 62, 81, and 96 nm after sintering, and are thus the initial particle size before oxidation. The sintered particles were then mixed with dry air with a 1:1 ratio, and enter a well-characterized tube reactor for oxidation at a controlled temperature (25–1100 °C). The oxidation reactor consisted of a quartz reactor tube of 1 cm i.d. and 120 cm long with a heated length of 36 cm. The axial temperature profiles along the quartz tube were measured at each selective temperature by using a thermocouple, and are shown in Figure 3. For the nominal operating condition of 1 LPM through the oxidation furnace, the residence time estimated from the measured temperature profiles gives ~ 1.3 s for room temperature to ~ 0.3 s at 1100 °C. A more detailed discussion for the measurement of temperature profile in the tube furnace and calculation of the resident time can be found in our previous work.^{36,44}

Finally the reacted particles are directed to the second DMA, or the APM, for the size and mass measurement. Transmission Electron Microscopy (TEM) was also used to examine the structure of nickel nanoparticles before and after sintering to evaluate the sintering process. An electrostatic precipitator was used after the reaction furnace to collect particles on Formvar coated 200 mesh copper TEM grids. TEM characterization was performed with a Zeiss EM10 TEM (accelerating voltage: 80 kV and magnification: $100\times$ – $200000\times$).

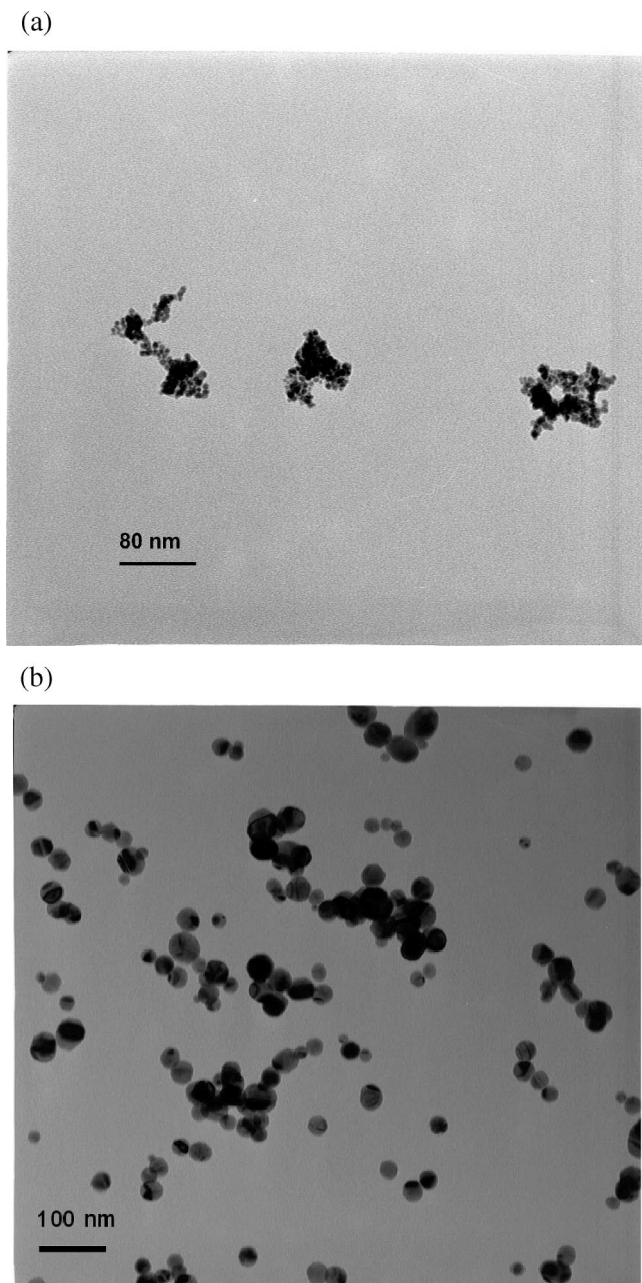


Figure 4. TEM micrographs of nickel samples: (a) before sintering (b) after sintering.

Results and Discussion

A. Size and Mass Measurements of Nickel Nanoparticle Oxidation. The morphology of nickel nanoparticles as they exit the generator is shown in Figure 4a and indicates the particles are highly aggregated with primary particles less than 5 nm. At the high oxidation temperatures, oxidation and sintering (which decreases surface area) would occur simultaneously for such small primary particle size, and make the measurements and subsequent data analysis too ambiguous. For this reason we choose to sinter the aggregates to spheres. TEM images of the polydisperse particles sampled after the sintering furnace are shown in Figure 4b and confirm that the aggregates were successfully sintered to form spheres. Note that the TEM sample was prepared by sintering polydisperse particles without DMA-1 selection, and although the sintering process would result in perfectly spherical particles without any aggregate structure,⁴⁷ the high concentration of generated particles leads to reaggre-

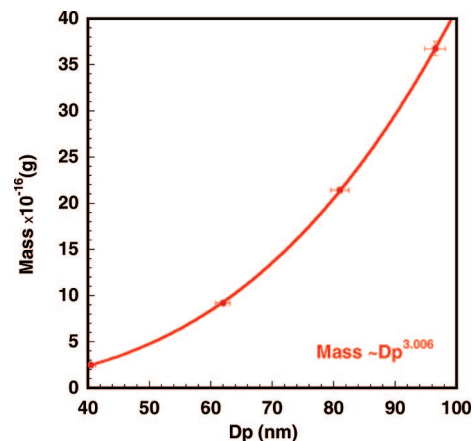


Figure 5. APM measured mass (Y axis) and TDMA measured initial particle size (X axis).

gation. This reaggregation can be prevented by first size selecting particles with DMA-1. Mobility sizes of 70, 135, 200, and 240 nm aggregate particles were selected, their size and mass after sintering were subsequently measured with DMA-2 and APM, and the results are shown in Figure 5. The particle sizes shrink to 40, 62, 81, and 96 nm after sintering and the measured mass (APM) and size (DMA) show a relationship of mass $\sim Dp^{3.006}$, implying that individual spherical nickel particles were obtained for the subsequent oxidation step.

We now turn to the size-selected measurements. Mobility size-selected Ni particles of 40, 62, 81, and 96 nm (after sintering) were mixed with air and oxidized, following which the size or mass of the reacted particles is measured by a second DMA or APM.

Panels a, b, c, and d of Figure 6 show normalized particle size distributions measured by DMA-2 at selected furnace temperatures for initial mobility size of 40, 62, 81, and 96 nm, respectively. The size distributions obtained for each furnace temperature were fit to a Gaussian distribution to determine the peak size. As mentioned above, the initial unreacted particle size is determined from DMA 2 at 25 °C. Furthermore, measurements of particle oxidation at 200 °C show no size change, indicating that reaction if there is any is below our detection limit, which we estimate from prior work to be ~ 0.3 nm in diameter.

The TDMA experimental results in Figure 6 show that the particle size first increases as we increase the furnace temperature, and reaches a size maximum at 600 (for particles with initial size 40 nm), 700 (for particles with initial sizes 62 and 81 nm), and 800 °C (for particles with initial size 96 nm). Further increases in the reaction temperature result in decreases in particle size as the peak size decreased from a maximum of 51.3 to 49 nm, 81.4 to 77.5 nm, 106.9 to 102.5 nm, and 124.8 to 121.8 nm for particles with initial sizes of 40, 62, 81, and 96 nm, respectively. The detailed particle peak size data are shown in Table 1, and the size change ΔDp as a function of furnace temperature is shown in Figure 7.

The TDMA experiment indicates that the oxidation starts at ~ 300 °C as evidenced by an increase in particle size. This size increase results because nickel oxidation forms a lower density oxide than the zerovalent metal. However, the size increase is not continuous in temperature, and in the higher temperature regions (above 600 °C), a significant size decrease is observed for all particle sizes. There are several possible reasons that can contribute to the shrinkage of particles at high temperatures. First, some particles are not perfectly spherical, and some may

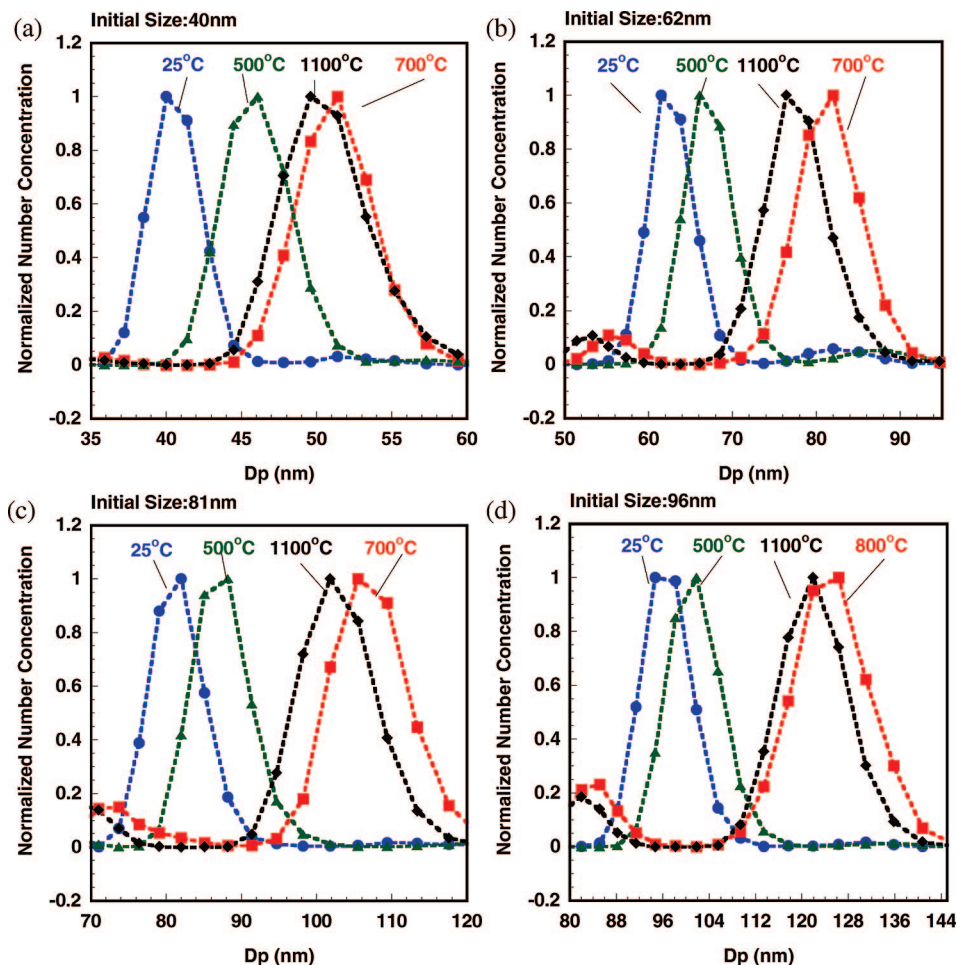


Figure 6. TDMA measured size distribution for initial size of (a) 40, (b) 62, (c) 81, and (d) 96 nm nickel particles at different oxidation temperatures.

TABLE 1: Change in Particle Size As a Function of Oxidation Temperature

furnace setting (°C)	particle size (nm)			
	40	62	81	96
25	40.0	62.0	81.0	96.6
200	40.0	62.0	81.0	96.6
300	40.2	62.5	81.3	96.9
400	41.5	63.6	81.8	97.5
500	45.9	67.0	87.1	101.2
600	51.3	77.9	95.8	110.2
700	51.2	81.4	106.9	122.7
800	50.9	81.2	106.9	124.8
900	50.1	80.7	106.5	124.7
1000	49.0	78.7	104.8	123.8
1100	50.3	77.5	102.5	121.8

be slightly aggregated, so that one may argue that what was seen at these temperatures is really sintering or rearrangement of particle morphology. However, as we have discussed above, this is an unlikely explanation considering the fractal dimension of the particles is ~ 3 based on the experimental result shown in Figure 5. As a result, any size change after particles pass through the oxidation furnace can be attributed solely to oxidation, e.g., not from the rearrangement of particle morphology.

The most likely explanation for our experimental observation (and consistent with APM results to be presented later) would be the formation of an intermediate phase of the oxide, Ni_2O_3 , at low temperatures, and further decomposition of Ni_2O_3 to NiO at higher temperatures. This is consistent with the fact that Ni_2O_3

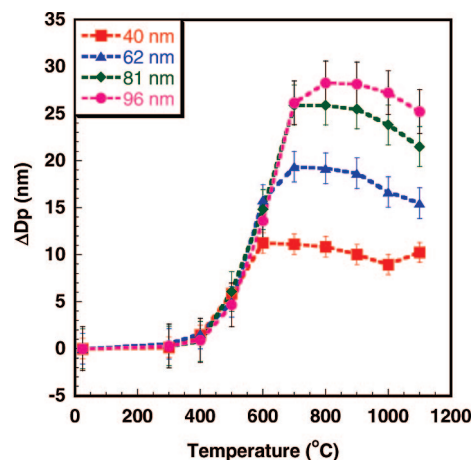


Figure 7. TDMA measured change of particle size as a function of oxidation temperature.

is the thermodynamically favorable phase at low temperature, and decomposes into NiO and oxygen at temperatures above 600 °C.

The reacted particle size can be estimated by assuming spherical particles of Ni completely convert to Ni_2O_3 or NiO. Our experimental values fall within this calculated size range. For example, for an initial 40 and 96 nm Ni particle, the particle size should increase to 55.6 and 132.6 nm for complete conversion to Ni_2O_3 , and then decrease to 48.3 and 115.2 nm upon forming NiO, while our experimental value for an initial

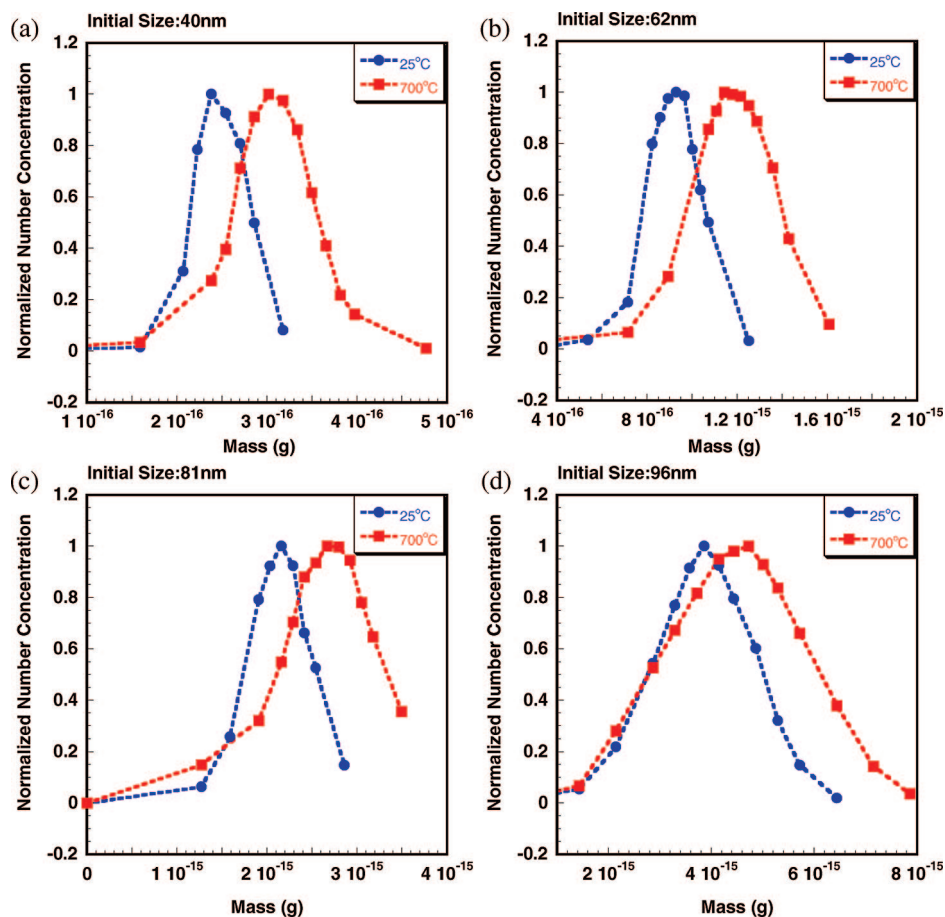


Figure 8. APM measured mass distribution for the initial size of (a) 40, (b) 62, (c) 81, and (d) 96 nm nickel particles at different oxidation temperatures.

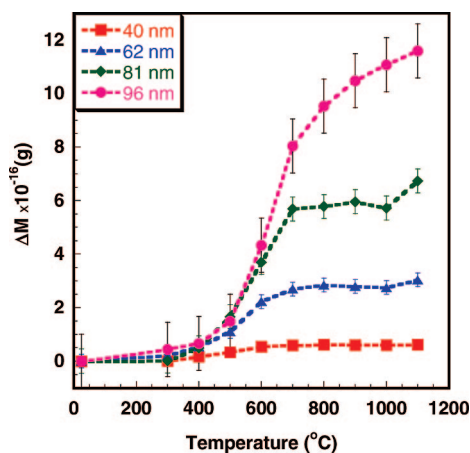


Figure 9. DMA-APM result for change of particle mass as a function of oxidation temperature.

40 nm particle increases to 51.3 nm at 600 °C, and then shrinks to 49 nm at 1000 °C. For an initial size of 96 nm particle the size is 124.8 nm at 800 °C and 121.8 nm at 1100 °C. Also these results show that the smaller the initial particle size, the closer we achieve to full conversion, while larger particles require a higher temperature to achieve full conversion.

To further investigate the oxidation of nickel nanoparticles and evaluate the phase behavior observed in the TDMA experiments, we substitute the APM for the second DMA to track particle mass changes due to oxidation. As discussed previously, the APM classifies particles by mass through a balance of electrostatic and the centrifugal forces.⁴⁰ For each

TABLE 2: Change in Particle Mass As a Function of Oxidation Temperature

furnace setting (°C)	particle mass ($\times 10^{-16}$ g)			
	40	62	81	96
25	2.48	9.19	21.43	36.81
300	2.50	9.40	21.44	37.25
400	2.65	9.73	21.93	37.40
500	2.82	10.29	23.10	38.30
600	3.03	11.42	25.12	41.15
700	3.08	11.89	27.12	44.85
800	3.11	12.03	27.21	46.34
900	3.10	11.98	27.39	47.28
1000	3.10	11.94	27.15	47.88
1100	3.11	12.23	28.16	48.40

particle mobility size, the APM was operated at a fixed rotation speed, and as such the applied voltage can be directly related to particle mass. Panels a. b. c. and d of Figure 8 show the results of the APM measured mass distribution at selected furnace temperatures for initial mobility sizes of 40, 62, 81, and 96 nm, respectively. Figure 9 shows the mass change ΔM as function of furnace temperature. Because the APM has a broader transfer function compared to that of the DMA, especially at the low end of the APM range, a plot of the experimental data for each temperature would overlap, and would be difficult to read. For this reason, we only show the experimental results at furnace temperatures of 25 and 700 °C. The particle peak mass distribution data at each furnace temperature were fit to a Gaussian function to obtain the peak mass and are shown in Table 2. It is clear from Figure 8 and Table 2 that there is a mass increase, with increasing furnace

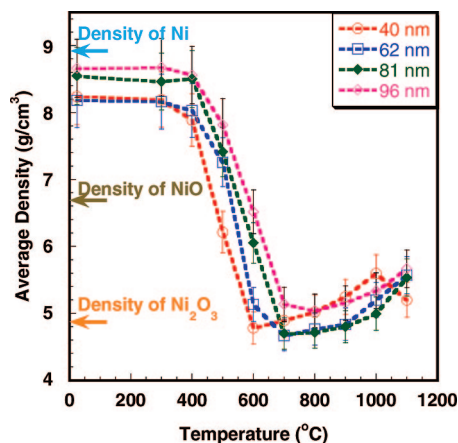


Figure 10. Average density measured with use of the DMA-APM combined experiment.

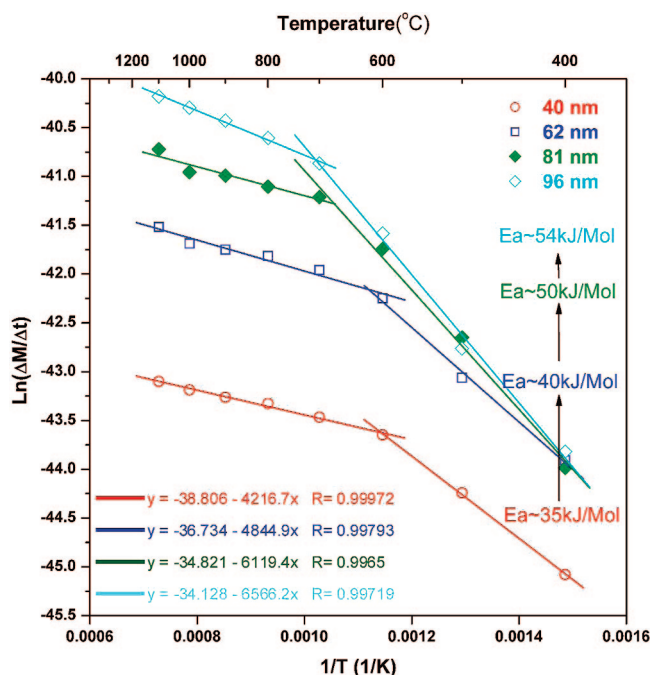


Figure 11. Arrhenius plots of average mass changing rate as a function of inverse temperature. The calculations for activation energy are only for the low-temperature region.

temperature, that reaches a maximum at above 600 °C. On the other hand, from Figure 9, we can see in the hypothesized phase change region that the measured value for the mass fluctuates within the experimental uncertainty for initial 40, 62, and 81 nm particles, and increases slowly with increased temperature for the initial 96 nm particle. As we discussed above, the theoretical particle size should grow to 55.6 and 136.6 nm for an initial 40 and 96 nm nickel particle, if we assume complete conversion, while the DMA measured value is 51.3 and 124.8 nm. This suggests that the nickel particle could act as a multicomponent oxide during the oxidation process.

Presumably the particle would have a nickel core with an outer oxide layer that contains both NiO and Ni₂O₃. Both the oxidation of the nickel core and decomposition of the outer Ni₂O₃ layer could occur simultaneously and result in a roughly constant particle mass as observed for small particles, and slow mass gain for large particles.

Our previous work showed that the APM when combined with TEM image analysis can accurately determine particle

density.³⁸ More recently, the DMA-APM technique was used as an online measurement tool to obtain the particle density in understanding aluminum oxidation.³³ In this work, the average density profiles of reacted particles are calculated by using the TDMA and APM measured particle size and mass and are shown in Figure 10. We find that as the furnace temperature increases, the average density of the reacted particles decreased monotonically to 4.7–5.0 g/cm³, consistent with the density of Ni₂O₃ (4.84 g/cm³).^{48,49} At higher temperatures the particle density increases to 5.5–5.7 g/cm³ and at the highest temperature investigated is roughly at a density halfway between that of NiO (6.67 g/cm³) and Ni₂O₃ (4.84 g/cm³). The oxidation to form Ni₂O₃ should be dominant in the low-temperature region while the process of formation of the two types of oxides and the phase transition are coupled at higher temperatures.

B. Size-Resolved Oxidation Kinetics of Nickel Nanoparticles. Metal oxidation theories and the transport properties of the oxides have been studied for several decades. It is believed that the diffusion of ionic vacancies and electron holes is the dominant transport process for nickel oxidation.⁷ Thus, the well-known diffusion-controlled shrinking core model^{15,51} can be employed to extract the reaction rate constant. The theories proposed by Wagner for thick film growth are based on conditions of charge neutrality, and diffusion of ions and electrons being the rate-limiting step, leading to a parabolic rate law for a planar geometry.²⁷ Carter later applied the same assumptions to the shrinking core model for a spherical geometry and derived an oxidation rate law for metal particle oxidation.²² However, Wagner's theory is restricted to thick films in which the characteristic length is given by the Debye–Hückel length, which is probably on the order of hundreds of nanometers.^{7,8,11} Given the particle sizes we are studying, many of the assumptions of the theory would likely be invalid. For example, the charge-neutrality condition of Wagner's theory would no longer hold due to the space charge effects. Cabrera and Mott's, on the other hand, describe the thin film growth²⁶ assuming thermal electron emission and tunneling of electrons to be easier than ionic diffusion, so that an electric field is developed across the thin film to assist the transport of the ions. The electric field caused by the surface-charge could be on the order of $\sim 10^7$ V/cm such that a nonlinear behavior has to be considered. The rate law for thin films was derived and a characteristic length L_{crit} was suggested, below which the field is so strong that the drift velocity of ions is not proportional to the field but has an exponential dependence, and this nonlinear effect should be considered when $L(t) < L_{\text{crit}}$. The upper limit for Cabrera and Mott's theory is ~ 10 nm for nickel, and L_{crit} is as small as 2 nm. No analytical result has been developed for the spherical geometry.

Fromhold and co-workers have given a more general theoretical model for metal oxidation.^{8,11,15,17,20} However, the equations can only be solved numerically. In our case, the particle sizes fall in the range between those of Wagner's theory and Cabrera and Mott's theory. Nickel nanoparticle oxidation is most likely in a low-field region where surface-charge and space-charge should be considered. Fromhold and Cook have evaluated the space-charge and surface-charge modification on the oxidation kinetics with a coupled current approach based on the idea that the diffusion currents are in the steady state in the presence of surface/space charge and the growth kinetics was obtained by summing the ionic and electronic diffusion currents of all the species.¹⁵ The results can only be solved numerically and no results are available for spherical particle oxidation.

TABLE 3: Summary for Arrhenius Parameters for Nickel Nanoparticle Oxidation

particle mobility size (nm)	temp range (°C)	curve fit parameters ($Y = aX + b$)		activation energy (kJ/mol)	effective diffusion coefficients (10^{-9} cm ² /s)
		a	b		
40	400–600	4216.7	−38.8	35.0 ± 0.8	0.56–4.64
62	400–600	4844.9	−36.7	40.3 ± 2.6	1.02–17.0
81	400–700	6119.4	−34.8	50.8 ± 3.0	0.27–33.7
96	400–700	6566.2	−34.1	54.6 ± 2.9	0.18–35.4
40	700–1100	1267.7	−42.2	10.5 ± 0.5	NA
62	700–1100	1336.9	−40.6	11.1 ± 1.5	NA
81	800–1100	1479.8	−39.7	12.3 ± 2.2	NA
96	800–1100	2085.3	−38.7	17.3 ± 0.4	NA

More recently Fromhold has developed a model focused on the oxidation rate of spherical metal particles in the low space charge limit using the coupled current approach for oxide thicknesses below 100 nm.⁶ Only surface charge and linear diffusion were considered in their study, and a rate law similar to that from Carter's work was obtained. This suggested to us that the diffusion-controlled shrinking core model could be applied to our study as a relatively straightforward way to process our experimental results.

Following Carter's analysis at steady state, the diffusion flux through the oxide shell can be related to the reaction rate of reactant by

$$\frac{dN_{O_2}}{dt} = -4\pi DeC_{O_2} \frac{r_1 r_2}{r_2 - r_1} \quad (1)$$

In eq 1, r_1 and r_2 are the radius of the nickel core and the reacted particle. C_{O_2} is the oxygen molar concentration in gas and N_{O_2} is the number of moles of oxygen in the oxide layer. De is the diffusion coefficient for ion diffusion in the oxide layer:

$$De = A_m \exp\left(-\frac{E_a}{RT}\right) \quad (2)$$

Here A_m is the pre-exponential factor, E_a is reaction activation energy, and R is the gas constant. Equation 1 immediately leads to the mass change rate for the reacted nickel nanoparticle, as

$$\frac{dM}{dt} = 4\pi M_{O_2} DeC_{O_2} \frac{r_1 r_2}{r_2 - r_1} \quad (3)$$

where M_{O_2} is the molecular weight of oxygen. Knowing the furnace temperature profiles from Figure 3, the particle mass change, ΔM can be obtained by integrating eq 3 as the particle travels down the oxidation furnace. However, as we discussed above, the nickel nanoparticle oxidation should be a composite

between formation of NiO and Ni₂O₃, and the phase transition. Therefore the relative concentration of NiO and Ni₂O₃ within the oxide layer is temperature dependent. As a result, the instantaneous mass changing rate dM/dt cannot be determined with our current experimental approach.

Considering the exponential temperature dependence of the rate constant and the fact that most of the reaction would occur at the center of the furnace at the peak temperature, we approximate the instantaneous mass changing rate dM/dt in eq 3 with the average mass changing rate to get

$$\ln \frac{\Delta M}{\tau} = -E_a/RT + \ln\left(4\pi M_{O_2} C_{O_2} A_m \frac{r_1 r_2}{r_2 - r_1}\right) \quad (4)$$

Here the peak temperature determined from Figure 3 is used, and by using the mass change measured from the APM, the average mass change rate can be calculate for each furnace temperature. The size-resolved activation energy can be obtained from an Arrhenius plot as shown in Figure 11. Considering that only very small mass changes were observed at 300 °C, we do not use results from that temperature to process the data. Two different regions can be distinguished from the Arrhenius plot, as the oxidation process transitions to a phase change region at ~600–700 °C. The kinetic parameters for both regions can be determined by using a linear fit. The curve fit parameter as well as the size-resolved activation energies obtained are summarized in Table 3 and the results for the low-temperature region are also shown in Figure 11. The calculated activation energies in the low-temperature region decrease from 54 kJ/mol to 35 kJ/mol as the particle mobility size decreases from 96 to 40 nm. The activation energies are significantly lower in the phase transition region, and further investigation is needed to understand this phase behavior. The activation energies obtained here (~0.4 eV) are considerably smaller than the value of 1.5 eV reported by Karmhag et al. for micro-size Ni particle oxidation and 1.34 eV for nano-size Ni particle oxidation,^{29,32} and also smaller than 1.78 eV for grain boundary diffusion limited thin film oxidation reported by Atkinson.⁷ This difference between conventional methods and our approach has been consistently observed in previous work.^{34,35} Moreover, the activation energies obtained here are much closer to the value of 0.6–0.9 eV for electron transport in single-crystal nickel oxide,⁵² and consistent with the reported activation energy of 0.3 eV for single-crystal Ni oxidation in the early film-thickening stage.⁵³ It is well-known that there are significant drawbacks of the conventional methods associated with the influence of experimental artifacts.⁵⁴ In those methods, usually milligrams of bulk sample are needed, while the sample mass of our aerosol-based techniques is ~1 fg. For a highly exothermic reaction such as the metal oxidation process, the large exotherm in a bulk sample will corrupt the observed onsite temperature, and the rapid reaction will lead to heat and mass transfer effect for bulk sample. As a consequence, the kinetic parameters

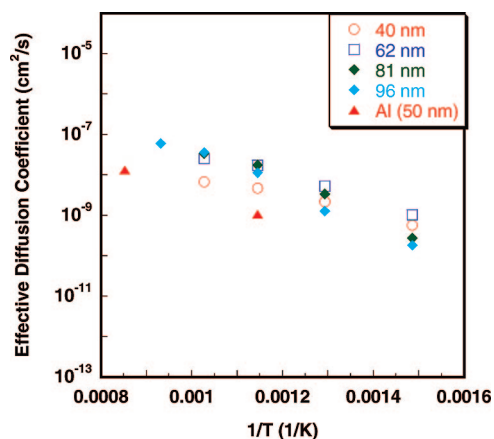


Figure 12. Arrhenius plot of effective diffusion coefficients in the low-temperature region for Ni and Al.

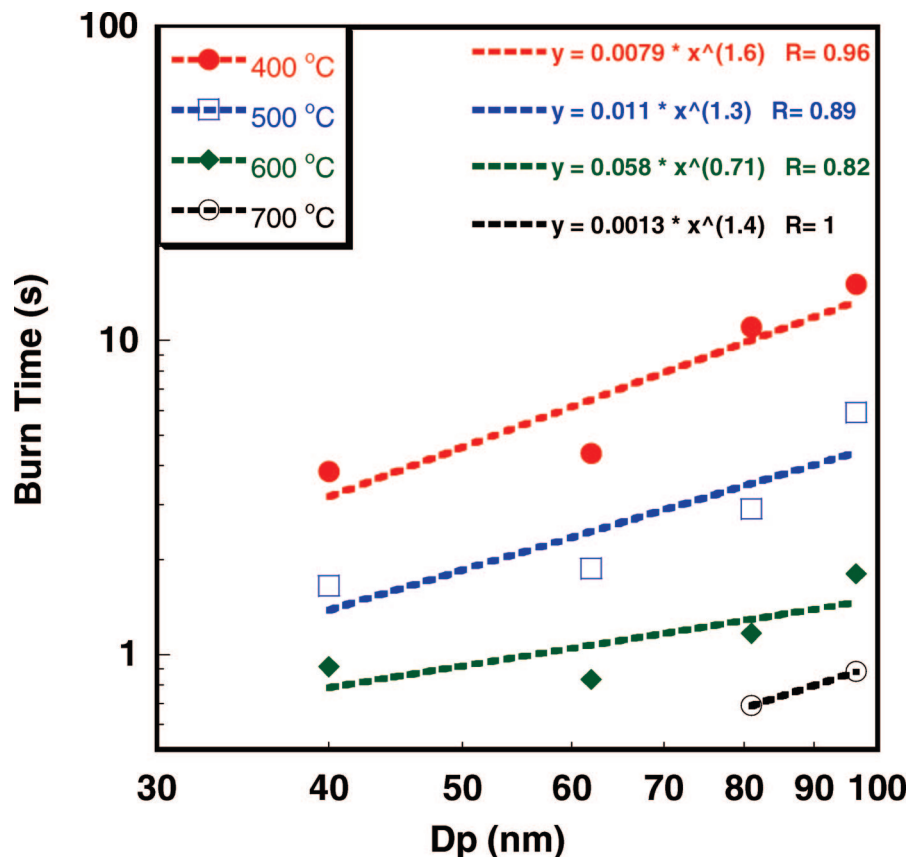


Figure 13. Particle burn time at different temperatures as a function of initial particle size.

extracted from the conventional methods are obscured. The TDMA and DMA-APM techniques employed here allow a direct measure of mass and volume change of individual particles, which enables us to explore the intrinsic reactivity of nanoparticles with minimizing the sampling error introduced by mass and heat transfer.

The effective diffusion coefficient is determined by calculating the unreacted nickel core radius r_1 . Although the oxide layer contains both NiO and Ni₂O₃ and their relative concentrations cannot be determined, the oxygen concentration is roughly uniform for NiO and Ni₂O₃. Calculation shows that the relative oxygen density in NiO is 1.42 g/cm³ and that in Ni₂O₃ is 1.40 g/cm³. The uniform oxygen density enables us to estimate the nickel core radius by using the mass change of the particle measured by the APM. Therefore the effective diffusion coefficient can be calculated from eq 3. Since the shrinking-core model used here can only count for the oxidation process, the phase transition in the high-temperature region will corrupt the calculation of the effective diffusion coefficient. As a consequence, the calculation is only valid in the low-temperature region, and the results are shown in Figure 12. Due to the well-known kinetic compensation effect, although the activation energy is considerably smaller than the value measured by the conventional offline methods, the measured diffusion coefficients are within the range of reported values.⁷ Since aluminum has been well studied and has been used extensively as a primary thermite-based material, the effective diffusion coefficients for aluminum oxidation obtained from our previous work³⁴ are also plotted in the figure for comparison. Surprisingly, the nickel is actually more active than aluminum although it should be pointed out that the aluminum measurements were made with a totally different experimental approach. However, despite the apparent faster kinetics of Ni, the higher enthalpy of aluminum

oxide (-1675.7 kJ/mol vs -489.5 kJ/mol for Ni₂O₃ or -239.7 kJ/mol for NiO)^{48,55} implies aluminum is still a more promising energetic material than nickel. Nevertheless, Ni might find applications as an ignition source, for example, or in tuning the reaction profile in mixed metal nanocomposites.

Particle burn time for different initial particle sizes at different temperatures was also calculated by using the burn rate and the total mass change measured from the APM. These results are plotted on a log scale in Figure 13, and show for all temperatures a diameter dependence well less than 2 ($\sim Dp^{1.4}$). For large size particles (micron size), the diffusion-controlled reaction would lead to a $\sim Dp^2$ dependence,⁵¹ and a $\sim Dp^{1.8}$ dependence is reported experimentally.⁵⁶ For nano-size particles, however, a much weaker size dependence has frequently been observed.^{56–58} A melt dispersion mechanism for very fast reaction of nanothermites was recently proposed to explain this observation.⁵⁷ Fast heating creates huge thermal stresses between the metal core and oxidation shell and results in the spallation of the shell and complete explosion of the core, the oxidation of dispersed metal clusters is much faster than diffusion and is independent of particle size. However, this mechanism is valid for particles with a melting core, and a solid shell, and is expected only for very fast heating rates ($\sim 10^7$ deg/s) as compared with our $\sim 10^3$ to 10^4 deg/s heating rates. A phenomenological model was developed for aluminum oxidation in our previous work,³³ which indicated that due to the internal pressure gradient in the particle, a $\sim Dp^{1.6}$ dependence was found. More generally, for the oxidation of metal, Formhold^{8,15} shows that a space charge layer in the growing oxide could have significant effects on the oxidation process for particles in the range of 10–100 nm, which can either retard or enhance the diffusion flux through the oxidation shell depending on ionic or electronic species as rate limiting.^{8,15} Our results for particle burn time

suggested that a model that includes both the pressure gradient and space charge effect would be worthy of investigation.

Conclusions

We applied online aerosol ion-mobility based methods to study oxidation and reactivity of nickel nanoparticles. The nickel nanoparticles were generated in situ during the oxidation experiments with use of gas-phase thermal pyrolysis of nickel carbonyl. Particles of well-controlled sizes and structure were generated and subsequently size selected by using a DMA. The mass and size changes of reacted particles were measured with an APM and a second DMA. The experimental data can be divided into an oxidation region and a phase transit region. On the basis of the diffusion-controlled rate equation in the shrinking core model, we found that the activation energy of oxidation decreased from 54 kJ/mol to 35 kJ/mol as the particle size decrease from 96 to 40 nm at low temperatures. The absolute burning time and the effective diffusion coefficient were also determined.

Acknowledgment. This work was supported by the Army Research Office.

References and Notes

- (1) Prakash, A.; McCormick, A. V.; Zachariah, M. R. *Nano Lett.* **2005**, *5*, 1357.
- (2) Park, K.; Rai, A.; Zachariah, M. R. *J. Nanopart. Res.* **2006**, *8*, 455.
- (3) Sullivan, K.; Young, G.; Zachariah, M. R. *Combust. Flame*. Submitted for publication.
- (4) Mrowec, S.; Grzesik, Z. *J. Phys. Chem. Solids* **2004**, *65*, 1651.
- (5) Rellinghaus, B.; Stappert, S.; Wassermann, E. F.; Sauer, H.; Spliethoff, B. *Eur. Phys. J. D* **2001**, *16*, 249.
- (6) Fromhold, J. A. T. *J. Phys. Chem. Solids* **1988**, *49*, 1159.
- (7) Atkinson, A. *Rev. Mod. Phys.* **1985**, *57*, 437.
- (8) Fromhold, A. T., Jr. *Theory of Metal Oxidation*; North-Holland Publishing Company: Amsterdam, The Netherlands, 1980; Vol. 2.
- (9) Sales, B. C.; Maple, M. B.; Vernon, F. L. *Phys. Rev. B* **1978**, *18*, 486.
- (10) Sales, B. C.; Maple, M. B. *Phys. Rev. Lett.* **1977**, *39*, 1636.
- (11) Fromhold, A. T., Jr. *Theory of Metal Oxidation*; North-Holland Publishing Company: Amsterdam, The Netherlands, 1976; Vol. 1.
- (12) Knutson, E. O.; Whitby, K. T. *J. Aerosol Sc.* **1975**, *6*, 443.
- (13) Graham, M. J.; Cohen, M. J. *Electrochem. Soc.* **1972**, *119*, 879.
- (14) Caplan, D.; Graham, M. J.; Cohen, M. J. *Electrochem. Soc.* **1972**, *119*, 1205.
- (15) Fromhold, A. T.; Cook, E. L. *Phys. Rev.* **1968**, *175*, 877.
- (16) Pizzini, S.; Morlotti, R. *J. Electrochem. Soc.* **1967**, *114*, 1179.
- (17) Fromhold, A. T.; Cook, E. L. *Phys. Rev.* **1967**, *163*, 650.
- (18) Fromhold, A. T., Jr.; Earl, L. C. *J. Appl. Phys.* **1967**, *38*, 1546.
- (19) Kazuo, F.; Bruce Wagner, J., Jr. *J. Electrochem. Soc.* **1965**, *112*, 384.
- (20) Fromhold, A. T., Jr. *J. Chem. Phys.* **1964**, *41*, 509.
- (21) Phillips, W. L., Jr. *J. Electrochem. Soc.* **1963**, *110*, 1014.
- (22) Carter, R. E. *J. Chem. Phys.* **1961**, *34*, 2010.
- (23) Gulbransen, E. A.; Andrew, K. F. *J. Electrochem. Soc.* **1957**, *104*, 451.
- (24) Gulbransen, E. A.; Andrew, K. F. *J. Electrochem. Soc.* **1954**, *101*, 128.
- (25) Dravnieks, A. *J. Am. Chem. Soc.* **1950**, *72*, 3761.
- (26) Cabrera, N.; Mott, N. F. *Rep. Prog. Phys.* **1948**, *12*, 163.
- (27) Wagner, C. Z. *Phys. Chem. Abt. B* **1933**, *21*.
- (28) Niklasson, G. A.; Karmhag, R. *Surf. Sci.* **2003**, *532*, 324.
- (29) Karmhag, R.; Niklasson, G. A.; Nygren, M. *J. Appl. Phys.* **2001**, *89*, 3012.
- (30) Karmhag, R.; Tesfamichael, T.; Wackelgard, E.; Niklasson, G. A.; Nygren, M. *Solar Energy* **2000**, *68*, 329.
- (31) Karmhag, R.; Niklasson, G. A.; Nygren, M. *J. Mater. Res.* **1999**, *14*, 3051.
- (32) Karmhag, R.; Niklasson, G. A.; Nygren, M. *J. Appl. Phys.* **1999**, *85*, 1186.
- (33) Rai, A.; Park, K.; Zhou, L.; Zachariah, M. R. *Combust. Theory Modell.* **2006**, *10*, 843.
- (34) Park, K.; Lee, D.; Rai, A.; Mukherjee, D.; Zachariah, M. R. *J. Phys. Chem. B* **2005**, *109*, 7290.
- (35) Mahadevan, R.; Lee, D.; Sakurai, H.; Zachariah, M. R. *J. Phys. Chem. A* **2002**, *106*, 11083.
- (36) Higgins, K. J.; Jung, H. J.; Kittelson, D. B.; Roberts, J. T.; Zachariah, M. R. *J. Phys. Chem. A* **2002**, *106*, 96.
- (37) Kim, S. H.; Fletcher, R. A.; Zachariah, M. R. *Environ. Sci. Technol.* **2005**, *39*, 4021.
- (38) Park, K.; Kittelson, D. B.; Zachariah, M. R.; McMurry, P. H. *J. Nanopart. Res.* **2004**, *6*, 267.
- (39) McMurry, P. H.; Wang, X.; Park, K.; Ehara, K. *Aerosol Sci. Technol.* **2002**, *36*, 227.
- (40) Ehara, K.; Hagwood, C.; Coakley, K. J. *J. Aerosol Sci.* **1996**, *27*, 217.
- (41) Sahoo, Y.; He, Y.; Swihart, M. T.; Wang, S.; Luo, H.; Furlani, E. P.; Prasad, P. N. *J. Appl. Phys.* **2005**, *98*, 054308/1.
- (42) He, Y. Q.; Li, X. G.; Swihart, M. T. *Chem. Mater.* **2005**, *17*, 1017.
- (43) Kim, S. H.; Zachariah, M. R. *J. Phys. Chem. B* **2006**, *110*, 4555.
- (44) Higgins, K. J.; Jung, H. J.; Kittelson, D. B.; Roberts, J. T.; Zachariah, M. R. *Environ. Sci. Technol.* **2003**, *37*, 1949.
- (45) Hinds, W. C. *Aerosol Technology: Properties, Behavior, and Measurement of airborne particles*, 2nd ed.; John Wiley & Sons, Inc.: New York, 1999.
- (46) Jung, H.; Kittelson, D. B.; Zachariah, M. R. *Combust. Flame* **2005**, *142*, 276.
- (47) Tsyganov, S.; Kastner, J.; Rellinghaus, B.; Kauffeldt, T.; Westerhoff, F.; Wolf, D. *Phys. Rev. B* **2007**, *75*.
- (48) ICT Database of thermochemical values; Fraunhofer Institut für Chemische Technologie: Pfingztal, Germany, 2001.
- (49) Antonsen, D. H.; Meshri, D. T. *Kirk-Othmer Encycl. Chem. Technol. (5th ed.)* **2006**, *17*, 106.
- (50) Smith, J. M. *Chemical Engineering Kinetics*, 3rd ed.; McGraw-Hill Inc.: New York, 1981.
- (51) Levenspiel, O. *Chemical Reaction Engineering*, 3rd ed.; John Wiley & Sons: New York, 1999.
- (52) Aiken, J. G.; Jordan, A. G. *J. Phys. Chem. Solids* **1968**, *29*, 2153.
- (53) Mitchell, D. F.; Graham, M. J. *Surf. Sci.* **1982**, *114*, 546.
- (54) Ortega, A. *International Journal of Chemical Kinetics* **2001**, *33*, 343.
- (55) CRC Handbook of Chemistry and Physics; Hampden Data Services Ltd., 2002.
- (56) Huang, Y.; Risha, G. A.; Yang, V.; Yetter, R. A. *Proceedings of the Combustion Institute* **2007**, *31*, 2001.
- (57) Valery, I. L.; Blaine, W. A.; Steven, F. S.; Michelle, P. *Appl. Phys. Lett.* **2006**, *89*, 071909.
- (58) Young, G.; Sullivan, K.; Zachariah, M. R. "Investigation of Boron Nanoparticle Combustion"; 46th AIAA Aerospace Sciences Meeting and Exhibit AIAA-2008 0942, 2007, Reno, Nevada.